Bulk synthesis of stoichiometric/meteoritic troilite (FeS) by high-temperature pyrite decomposition and pyrrhotite melting

Moreau, Juulia-Gabrielle

2022-03

Moreau , J-G , Joeleht , A , Aruvali , J , Heikkila , M J , Stojic , A N , Thomberg , T , Plado , J & Hietala , S 2022 , ' Bulk synthesis of stoichiometric/meteoritic troilite (FeS) by high-temperature pyrite decomposition and pyrrhotite melting ' , Meteoritics and Planetary Science , vol. 57 , no. 3 , pp. 588-602 . https://doi.org/10.1111/maps.13782

http://hdl.handle.net/10138/342350
https://doi.org/10.1111/maps.13782

The Meteoritical Society

Meteoritics & Planetary Science 57, Nr 3, 588–602 (2022)
doi: 10.1111/maps.13782

Bulk synthesis of stoichiometric/meteoritic troilite (FeS) by high-temperature pyrite decomposition and pyrrhotite melting

Juulia-Gabrielle MOREAU[1]*, Argo JÕELEHT[1], Jaan ARUVÄLI[1], Mikko J. HEIKKILÄ[2], Aleksandra N. STOJIC[3], Thomas THOMBERG[4], Jüri PLADO[1], and Satu HIETALA[5]

[1]Department of Geology, Institute of Ecology and Earth Science, University of Tartu, Ravila 14A, Tartu 50411, Estonia
[2]Department of Chemistry, University of Helsinki, P.O. Box 55 (A.I. Virtasen aukio 1), FI-00014, Finland
[3]Institut für Planetologie, Westfälische Wilhelms Universität Münster, Wilhelm-Klemm-Str. 10, Münster 48149, Germany
[4]Institute of Chemistry, University of Tartu, Ravila 14A, Tartu 50411, Estonia
[5]Geological Survey of Finland, Neulamäentie 5, Kuopio FI-70211, Finland
*Corresponding author. E-mail: juulia.moreau@ut.ee

(Received 07 July 2021; revision accepted 16 December 2021)

Abstract–Stoichiometric troilite (FeS) is a common phase in differentiated and undifferentiated meteorites. It is the endmember of the iron sulfide system. Troilite is important for investigating shock metamorphism in meteorites and studying spectral properties and space weathering of planetary bodies. Thus, obtaining coarse-grained meteoritic troilite in quantities is beneficial for these fields. The previous synthesis of troilite was achieved by pyrite or pyrrhotite heating treatments or chemical syntheses. However, most of these works lacked a visual characterization of the step by step process and the final product, the production of large quantities, and they were not readily advertised to planetary scientists or the meteoritical research community. Here, we illustrate a two-step heat treatment of pyrite to synthesize troilite. Pyrite powder was decomposed to pyrrhotite at 1023–1073 K for 4–6 h in Ar; the run product was then retrieved and reheated for 1 h at 1498–1598 K in N_2 (gas). The minerals were analyzed with a scanning electron microscope, X-ray diffraction (XRD) at room temperature, and in situ high-temperature XRD. The primary observation of synthesis from pyrrhotite to troilite is the shift of a major diffraction peak from ~43.2°2θ to ~43.8°2θ. Troilite spectra matched an XRD analysis of natural meteoritic troilite. Slight contamination of Fe was observed during cooling to troilite, and alumina crucibles locally reacted with troilite. The habitus and size of troilite crystals allowed us to store it as large grains rather than powder; 27 g of pyrite yielded 17 g of stochiometric troilite.

INTRODUCTION

Iron sulfides play an essential role in understanding the Earth interior and accretional processes of planetesimals at the dawn of the solar system (Brown et al., 1984; Dibb et al., 2021; Fujita et al., 1999; Hirata et al., 1995; Lehner et al., 2010; Louzada et al., 2010; Mare et al., 2014; Morard et al., 2007, 2011; Tomkins, 2009; Xie et al., 2014). They are major components of Earth rocks, chondrites (Lunning et al., 2019; McSween et al., 1991), iron meteorites (Oshtrakh et al., 2016), and achondrites (e.g., Martian meteorites, Rochette et al., 2001). Iron sulfides exist within a solid solution in the Fe-S system (Mare et al., 2014; Sharma & Chang, 1979; Tomkins, 2009; Waldner & Pelton, 2005) with the two principal sulfide endmembers: pyrite (FeS_2) crystallizing in the cubic and troilite (FeS) in the hexagonal systems (stoichiometric pyrrhotite [$Fe_{1-x}S$] where $x = 0$). Whereas pyrite and pyrrhotite are either found in oxidizing or reducing environments, stoichiometric troilite is only stable in reducing environments and, thus, is rarely found in its pure form on Earth. Troilite with Fe/S ratio between 0.97 and 1.00 is characteristic in H, LL, LL chondrites and a few carbonaceous

chondrites (Schrader et al., 2021). Because troilite is abundant in planetary rocks other than on Earth, its study and direct observation are important.

Recent studies had a particular focus on shock metamorphism in ordinary chondrites (OCs) (Stöffler et al., 2018), where troilite plays a vital role as a marker of impact events (Kohout et al., 2014, 2020; Moreau et al., 2017, 2018, 2019; Moreau & Schwinger, 2021). The average troilite modal abundance in OCs is 5.5–5.9 wt% (McSween et al., 1991) or ~5 vol% (Hutchison, 2007). The shock melting and migration of troilite melt into solid silicates, from high shock pressures (>40 GPa), darkens the lithology of OCs (Britt & Pieters, 1989, 1994; Britt et al., 1989; Heymann, 1967; Keil et al., 1992; Kohout et al., 2014; Stöffler et al., 1991). The interest in reproducing this darkening in laboratory experiments in a controlled environment is high, because, on the one hand, ultraviolet, visible, near infrared (UV/Vis/NIR) and mid-infrared (MIR) spectra are essential to understand impact processes in the solar system and the distribution of asteroids in the Main Belt (DeMeo et al., 2009; DeMeo & Carry 2014; Güldemeister et al., 2021), and on the other hand, spectral properties of iron sulfides, and troilite in particular (Dibb et al., 2021), are an important asset for the study of planetary surface spectral properties and space weathering in general (Kracher & Sears, 2005; Matsumoto et al., 2020). Space weathering research, where physical samples of planetary or asteroidal surfaces are often not available for direct laboratory measurements, also focuses on experiments that are conducted with analog materials and rocks (e.g., Morlok et al., 2020). In order to simulate the asteroidal or planetary surface composition in an authentic way, genuine mineral phases and rocks must be used. Genuine troilite comparable to the meteoritic troilite is hardly available on Earth; therefore, such research would benefit from obtaining troilite material produced at low costs and as coarse grains.

In previous studies, the synthesis of pyrrhotite ($Fe_{1-x}S$) or troilite (FeS) was achieved using chemical (Akhtar et al., 2013; Pedoussaut & Lind, 2008; Roberts et al., 2018) or thermal treatment (Boyabat et al., 2003; Coats & Bright, 1965; de Oliveira et al., 2018; Onufrienok et al., 2020; Selivanov et al., 2008; Xu et al., 2019). For example, the synthesis of pyrrhotite by heating pyrite at high temperature (<1100 K) in CO_2 or N_2 atmosphere (Boyabat et al., 2003; de Oliveira et al., 2018) or the synthesis of troilite from pyrite at higher temperature under vacuum (1200 K; Onufrienok et al., 2020) was successfully achieved. However, the troilite obtained (quantities not readily known) at higher temperature (1200 K) was not entirely synthesized and X-ray diffraction (XRD) analyses showed the presence of several pyrrhotite compositions ([$Fe_{1-x}S$] with x = 0.125 and 0.025) in addition to troilite; the use of a vacuum may not have allowed the complete evacuation of sulfuric gas. Any high-temperature procedure reported in literature included chemical cleaning of the pyrite samples (acetone, HCl leaching, and other chemical treatments), careful preparation of grain sizes, and the use of tiny quantities of material at a time. The systematic study from Boyabat et al. (2003) investigated the influence of gas flow, grain size, temperature, and the exact time of high-temperature exposure. Forty-minute tests at 853–1023 K were identified as ideal experimental parameters for troilite synthesis at a gas flow of 1670 cm min^{-1} and grain sizes below 0.0548 cm. Similar conditions were reproduced by de Oliveira et al. (2018), who also noticed that pyrite oxidation occurs in CO_2 atmosphere and that pyrrhotite specimens remain very porous after decomposition. For chemical synthesis (e.g., Pedoussaut & Lind, 2008), near stoichiometric troilite was obtained, but in minimal quantities (e.g., nanoparticles; Roberts et al., 2018).

In this article, we propose to revisit high-temperature treatment procedures with the addition of induced melting above the melting point of troilite (1465 K) after having produced pyrrhotite from pyrite decomposition (Boyabat et al., 2003). By doing so, we wish to:

1. reduce the porosity at the grain scale by melting the mineral product;
2. allow for large quantities of pyrite to be treated, so the troilite product can be batched and used for various experiments (e.g., shock recovery experiments, Langenhorst & Deutsch, 1994, Langenhorst & Hornemann, 2005; spectral analyses for planetary surface characterization and melt migration tests within chondritic-like rocks, Moreau et al., 2021);
3. offer a simplified approach because controlled environments (gas flow, grain size, custom tube furnaces) are often difficult to obtain in general;
4. obtain troilite, as the stoichiometric mineral FeS, and compare our results with natural troilite from meteorites to validate its meteoritical properties; and
5. lead to the complete synthesis of troilite and avoiding pyrrhotite by-products through longer heat treatment and purging of excess sulfur.

In this study, we provide a thorough characterization of the produced pyrrhotite and troilite using scanning electron microscope (SEM) and in situ high-temperature x-ray diffraction. We compiled analyses to characterize the grain shape and surface, identified contamination products, and observed corrosive interactions with the sample holder. Furthermore, we performed XRD analyses to compare the troilite product to the pyrrhotite

product and natural meteoritic troilite. Additionally, we provide structural and spectral in situ analyses of the pyrrhotite-to-troilite transition process using X-ray and spectral analytical tools in tube furnaces. To offer more flexible experimental conditions, we will also enhance the thermal treatment by applying longer test durations, higher temperatures, and sample quantities, in contrast to more controlled experiments (Boyabat et al., 2003; de Oliveira et al., 2018; Onufrienok et al., 2020). We provide these details to ensure relatively easy synthesis procedures to guarantee that troilite is reproduced in standardized quality for any planetary science application.

MATERIALS AND METHODS

Pyrite Decomposition Procedure

For the study, we used fresh pyrite crystals from Navajún, Spain; they were provided by the University of Tartu Natural History Museum (TUG 1608-6992-3, -5, -7) with masses of 40.2, 14.6, and 12.9 g, respectively. After grinding the pyrite crystals in an agate mortar, we rinsed the powder several times with HCl 6 M followed by ethanol (using filters) and dried the mixture overnight at 373 K. Each sample batch was vacuum sealed.

Some amounts of powder were placed in quartz ceramic boats inserted in the middle of a glass tube fitting a horizontal tube furnace. Oxygen was purged for an hour with an Ar gas flow (18 L h^{-1}) before slowly heating (5 K min^{-1}) of the samples, which were then kept at 653 K for an hour to purge pyrite from oxygen elements (Boyabat et al., 2003). With continuous Ar flow, the heat was then slowly increased (between 2 and 10 K min^{-1}) to a maximum temperature of 1023–1073 K and kept at this level for 4–6 h. The samples were cooled at a rate of 5 K min^{-1}, then retrieved and immediately vacuum sealed.

Pyrrhotite Melting Procedure

The decomposed pyrites were placed in alumina (Al_2O_3) crucibles, which were inserted in a high-temperature tube furnace (Carbolite Gero 30–3000 °C) that was continuously flushed either with Ar or N_2 gas (20 L h^{-1}). The assemblage was oxygen purged for 1 h and subsequently heated at a rate of 10 K min^{-1}. The samples were kept at 1498–1598 K for 1 h before cooling them at a rate of 5 K min^{-1}. The samples were retrieved when the oven temperature readings indicated room temperature (298 K). All samples were immediately vacuum sealed.

The decomposition and melting procedures are summarized in Fig. 1.

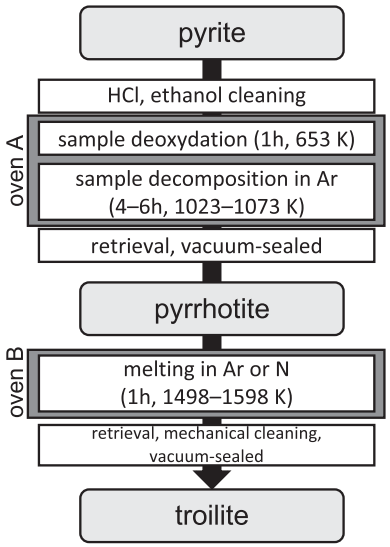

Fig. 1. Procedure for synthesizing troilite from pyrite, using two ovens.

Analysis of Samples

Pyrite, decomposed pyrite, and melted pyrrhotite were analyzed. The powder samples were studied by XRD using the Bruker D8 Advance diffractometer with Ni-filtered Cu Kα radiation. Scanning steps of 0.013°2θ from 10 to 97°2θ and a total counting time of 522 s per step were used. The diffraction patterns were analyzed using the Diffrac.EVA software with ICDD Powder Diffraction database PDF4+ (2020) and the full profile analysis software Topas 6 (Bruker, Germany).

To produce SEM-BSE (backscattered electron) images of our samples, we used a variable pressure Zeiss EVO MA15 SEM equipped with an Oxford X-MAX energy-dispersive detector system (EDS). Spectra were collected using 20 keV accelerating voltage and focused electron beam, then processed by the Aztec software.

We also carried out an in situ high-temperature XRD (HTXRD) analysis of the pyrrhotite sample using an Anton-Paar HTK1200N furnace attached to a PANalytical X'Pert Pro MPD diffractometer (up to 1473 K). This was done to observe any structural changes in the pyrrhotite and compare the transformation with the general procedure applied in this article. All measurements were conducted using a 10 mm mask, with a programmable divergence slit set to 8 mm length and a programmable antiscatter slit set to ensure the observation of the same sample portion. A PIXcel detector in 1-D mode was used for detecting the scattered radiation, and the pulse height discrimination range was narrowed to reduce the fluorescence caused by iron in the sample. Prior to the measurements, the furnace was heated for 2 h at 575 K in 1e-5 mbar pressure to dispose the moisture absorbed on the

Table 1. Samples, decomposition, and melting procedures.

			Decomposition[a]							Melting[b]				
Sample	Pyrite	Note	Quantity (g)[c]	Heating (K min^{-1})	Deoxidation (K)	Time (min)	Heating (K min^{-1})	Decomposition (K)	Time (min)	Quantity (g)[c]	Gas	Heating (K min^{-1})	Melting (K)	Time (min)
Troilite1-1	TUG 1608-6992-7	<0.20 mm	5	5	653	45	10	1023	240	0.4	Ar	10	1498	60
Troilite1-2	TUG 1608-6992-7	0.20–0.32 mm	2	5	653	45	10	1023	240	0.4	Ar	10	1498	60
Troilite1-3	TUG 1608-6992-7	>0.32–0.50 mm	4	5	653	45	10	1023	240	0.4	Ar	10	1498	60
Troilite2-1	TUG 1608-6992-7	<0.20 mm	Using same decomposed pyrrhotite for troilite1							0.4	N_2	10	1598	60
Troilite2-2	TUG 1608-6992-7	0.20–0.32 mm								0.2	N_2	10	1598	60
Troilite2-3	TUG 1608-6992-7	>0.32–0.50 mm								0.4	N_2	10	1598	60
Troilite3-1	TUG 1608-6992-3	Unsorted	8	5	653	60	2	1073	360	~5	N_2	10	1598	60
Troilite4-1	TUG 1608-6992-3	Unsorted—grinded for melting	27	5	653	60	2	1073	360	~25[d]	N_2	10	1598	60
Troilite5-1	TUG 1608-6992-5	Unsorted	11	5	653	60	2	1073	360	In situ high-temperature X-ray diffraction				

[a]Argon, 18 L h^{-1} gas flow, 1 h oxygen purge, 5 K min^{-1} cooling.
[b]20 L h^{-1} gas flow, 1 h oxygen purge, 5 K min^{-1} cooling.
[c]Quantity of pyrite (decomposition) and pyrrhotite (melting) inserted in the oven before heating.
[d]17.34 g of troilite recovered from alumina crucible.

porous furnace walls. The measurements on the pyrrhotite sample were conducted first at 298 K, then at 373 K, followed by measurements at 50 K intervals up to 1473 K. At the highest temperature, five measurements were conducted for 1 h. The sample was then cooled symmetrically back to room temperature. Longer measurements with a wider angular range were performed at 298 K before and after heating. The height position of the sample was automatically adjusted by the furnace software, but changes at the correct surface position are unavoidable after melting and recrystallization of the sample.

RESULTS

Decomposition and melting tests are compiled in Table 1. During these tests, two heating rates for decomposition, as well as two heat exposure durations for melting, and distinct inert gas species were applied in the ovens. In Figs. 2–7, we illustrate several aspects of the resulting decomposition and melting of pyrite and pyrrhotite. For tests labelled troilite1, troilite2, and troilite4, we provide SEM-BSE analyses with density maps (Figs. 5–7) of selected samples and BSE spectra qualitative analyses (Research Data). For tests labelled troilite1, troilite3, troilite4, and troilite5, we provide XRD analyses (Figs. 8–10). For the test labelled troilite5, we offer HTXRD results (Fig. 11).

Decomposition and Melting

Desulfurization of pyrite (FeS_2) to pyrrhotite ($Fe_{1-x}S$) is reactive at the conditions imposed in the oven as seen in Fig. 2. The loss of sulfur leads to a loss of mass. Decomposition of pyrite (troilite4) led to a net loss of 6.6146 g on a 27.6519 g powdered pyrite sample, a loss of ~90% of the total sulfur content of pyrite from a hypothetical loss of 7.3904 g; pyrite (troilite5) had a ~91% loss of sulfur content. Decomposition of pyrite to pyrrhotite is also macroscopically observable by the darkening of the mineral (Fig. 2).

Melting of pyrrhotite (Fig. 3a) is heavily pronounced with the formation of troilite as brownish-golden nuggets (Fig. 3b). Cavities likely formed owing to degassing (Figs. 3c and 3d) of trapped inert gas during melting. A darker and rough crust at the surface of troilite is observed (Figs. 3c, 3d, and 3f). Similar dark and rough droplets cling on the walls of the alumina crucible (Fig. 3e). Thermal treatment of troilite within alumina crucibles may weaken the crucibles because some broke upon cooling and retrieval. Melting of larger quantities of pyrrhotite (~20 g, troilite4-1) leads to visible surficial contamination (Figs. 4b, 4d, and 4e) and precipitation of sulfur minerals at the outlet of the gas flow (Fig. 4c). The

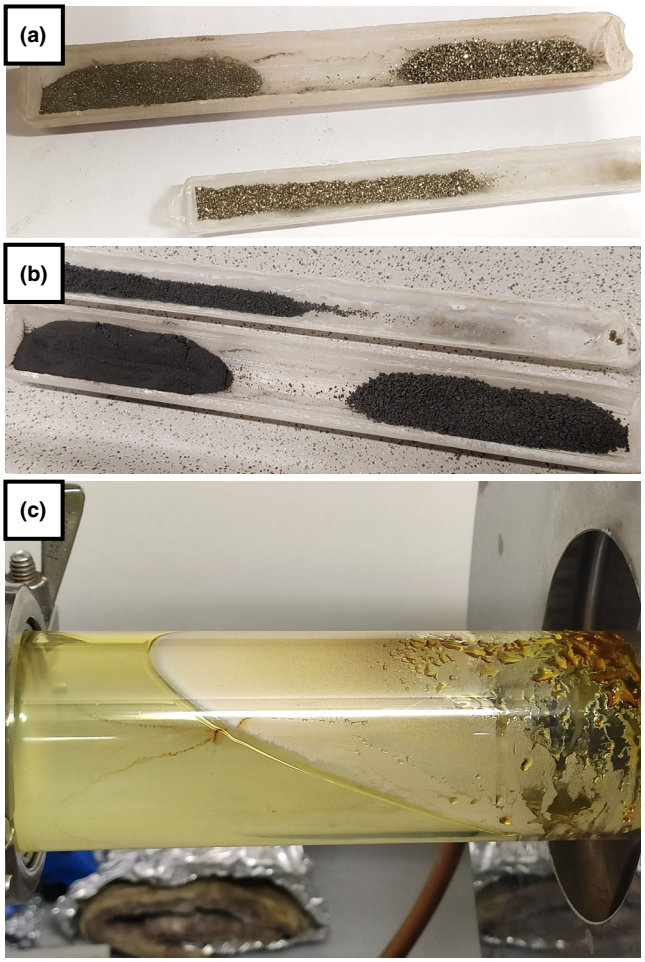

Fig. 2. The synthesis of troilite is a two-step process. It is safer to slowly decompose pyrite (a) into pyrrhotite (b) before melting the final product in another oven. The desulfurization of pyrite can be damaging to an oven if not protected accordingly as seen in (c), where a glass tube is used to safely purge the sulfur gas. (Color figure can be viewed at wileyonlinelibrary.com.)

contamination shown in Figs. 4b, 4d, and 4e consists of needle-shaped minerals outgrowing from the crucible walls or from a gray and porous residue at the surface of the sample ("cap," Fig. 4b.1; Fig. 7 where the porous element is displayed from beneath). Dendritic-shaped minerals also grew along with the needle minerals outward of the gray residue. The melted product is exposed after cleaning the surface, revealing coarse-grained crystals, when the crucible is forcefully opened. In this case, 17.34 g of the mineral was recovered, starting from an initial weight of pyrite of 27.65 g.

SEM-BSE Observations

Pyrite, pyrrhotite, and troilite all have very distinct features. From decomposition, pyrrhotite is highly

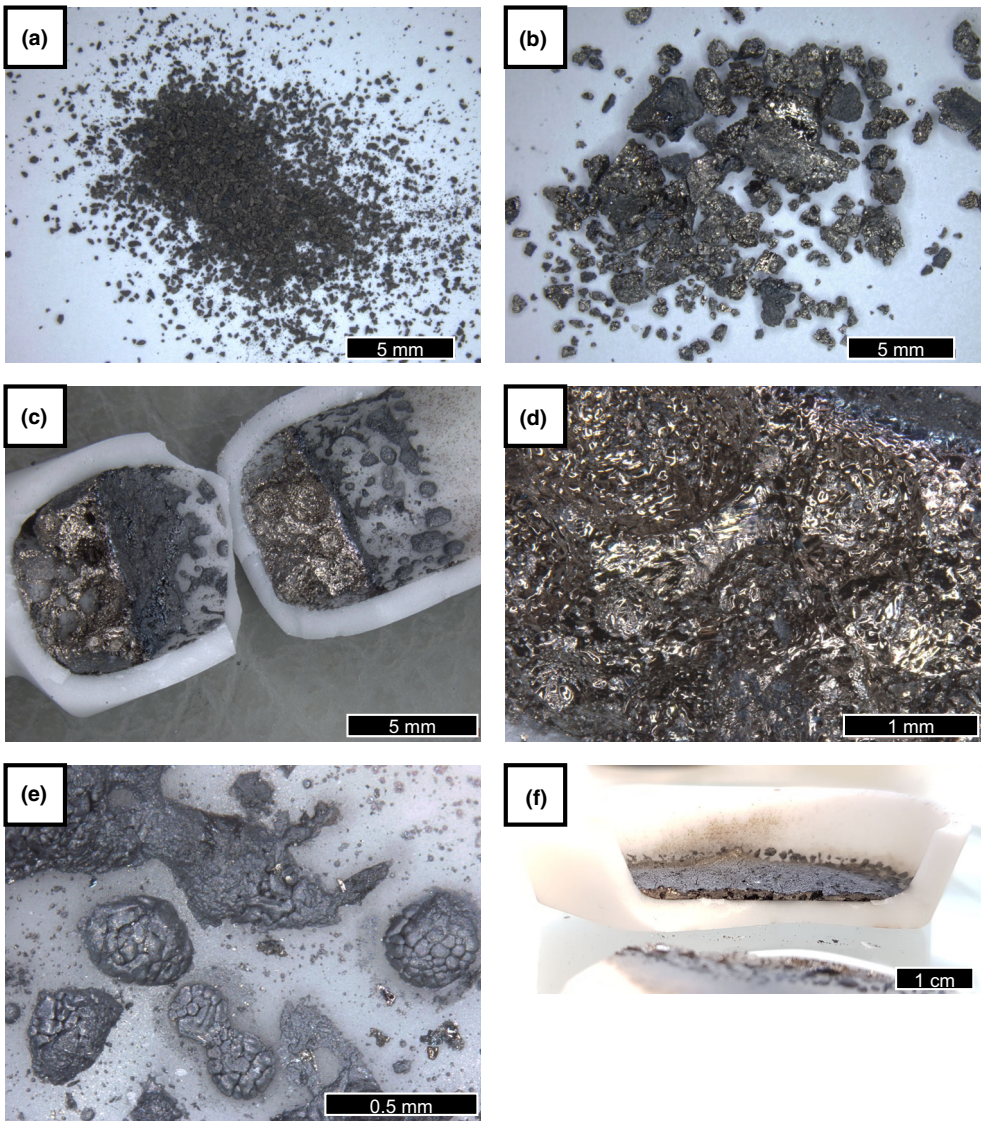

Fig. 3. Pictures taken from a Leica M205-A microscope: (a) pyrrhotite powder (0.3–0.5 mm grains) used to synthesize (b) troilite (troilite1-1); (c) troilite (troilite2-2) in its alumina crucible with (d, e) close-ups of the recrystallized melt and its crust, respectively. Picture of (f) troilite (troilite3-1) in its alumina boat crucible. a) Pyrrhotite melted to form (b) a brownish-gold colored troilite. The recrystallized troilite in (c, d) shows cavities from trapped gas and (e) a darker crust that has a rougher surface compared to the recrystallized troilite beneath. (Color figure can be viewed at wileyonlinelibrary.com.)

porous (Fig. 5b), depicting pitting-like alteration after desulfurization of the sample in the oven, distinguishing it from pyrite, and illustrating mass loss. Cracks allow us to see that this pitting goes deep into the pyrrhotite grain, giving it a coral-like appearance. The pyrite image in Fig. 5a shows that phyllosilicates can also coexist within pyrite, but we rarely observed such occurrences.

The formation of troilite and its textural features is diverse. Troilite displays different shapes such as aggregates of crystals (Figs. 5c and 5d), single angular crystals (Fig. 7f), and rounded crystals (Figs. 5d and 6b). Exsolutions of Fe-metal are observed such as droplets on surface of troilite (Fig. 6a), crystallized grains (Figs. 5d and 6a), skeletal growths (Fig. 5d), and larger deposits on the walls of the crucibles with higher concentration of sulfur (Figs. 6e and 6f). Contamination of Al_2O_3 in troilite, and/or iron, is observed at crust level or the crucible wall above it (Figs. 6d and 6f), at the contact between the troilite grain and the crucible wall (Figs. 6a and 6c), or as tiny inclusions in the round-shaped troilite (Fig. 6b). Occasionally, we also observed a lining of troilite on needle-shaped alumina crystals (Fig. 5f). Corrosion of the alumina crucible is

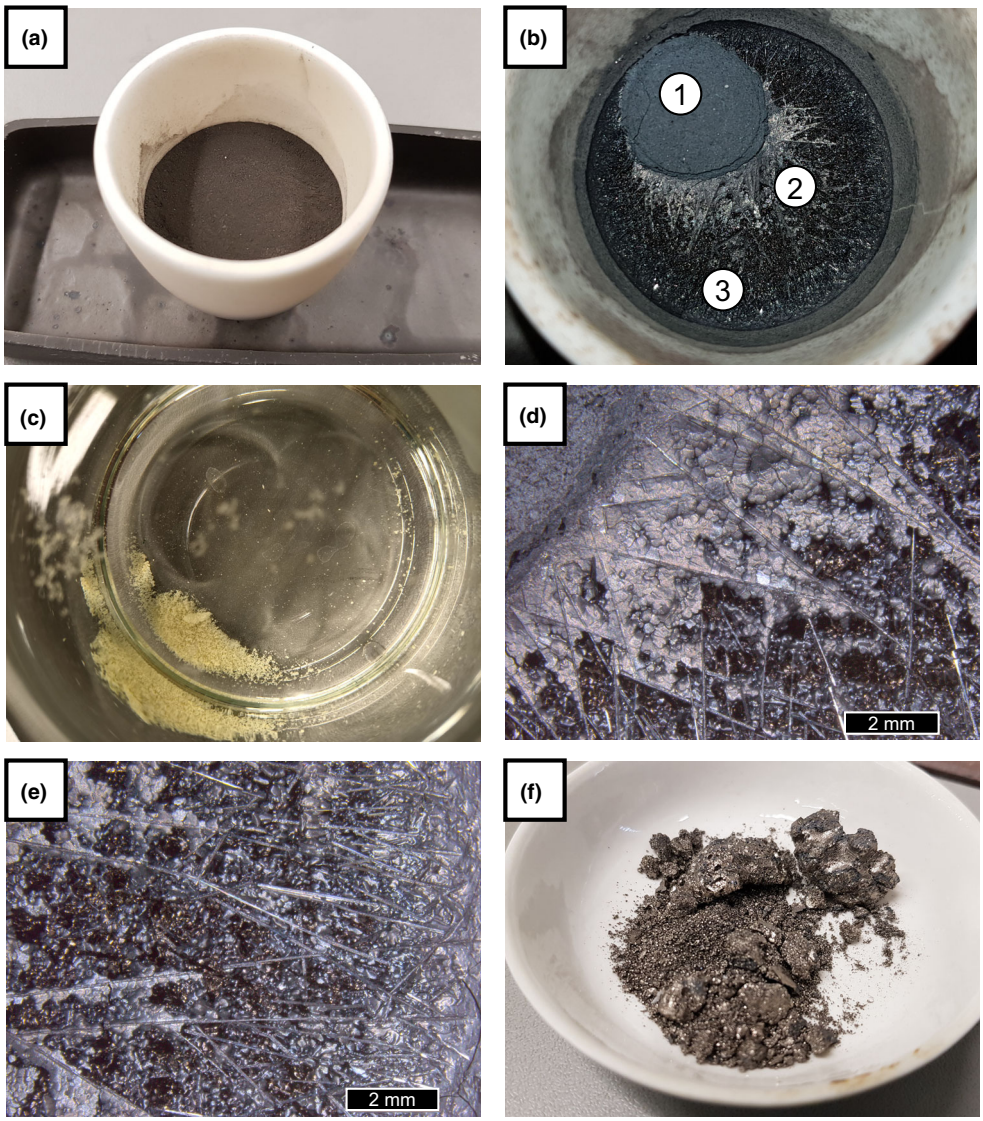

Fig. 4. Troilite (troilite4-1) synthesis pictures taken from phone and a Leica M205-A microscope: (a) grinded pyrrhotite powder used to synthesize troilite in alumina crucible; (b) surface contamination of troilite after melting at 1598 K; (c) oven outlet sulfur precipitation; (d, e) close-ups of the surface contamination made up of needle-shaped minerals (B.2, B.3) and dendritic growths (B.2) along needle-shaped minerals nearby and away from the contamination "cap" (B.1), respectively; (f) recovered troilite from beneath the surficial contamination for a total of ~17g. Troilite appears as a brownish-gold surface in (d, e). Needle-shaped minerals displayed in (b), (d), and (e) are semi-transparent and are radially oriented outward from the crucible walls and from the contamination "cap." The contamination "cap" seen in (b) was retrieved and had a pumice-like appearance. (Color figure can be viewed at wileyonlinelibrary.com.)

visible in some places (Fig. 5e). Whereas exsolution of Fe-metal happens within the troilite crystallized melt, Al_2O_3 contamination only happens at crucible walls or the surface of the crystallized melt. Further analyses of troilite4-1 (Fig. 7) show that the needle-shaped mineral contamination atop the melt is titanium oxide minerals with a coating of Fe-metal or iron sulfide. The porous element, which sat atop the melt (Fig. 4) and shown in Figs. 7a–c, is composed mainly of Al_2O_3, with minor troilite inclusions. The dendritic minerals observed in Fig. 4d could not be readily observed in SEM-BSE. The upper layer right beneath the surface of troilite4-1 is mainly composed of troilite grains (Fig. 7f).

X-Ray Diffraction

In Fig. 8, the sequence of analyses of pyrite (TUG 1608-6992-7) over pyrrhotite to troilite is shown from the same series of decomposition and melting (troilite1-1,2,3). Pyrite, pyrrhotite (pyrrhotite-11T, approx.

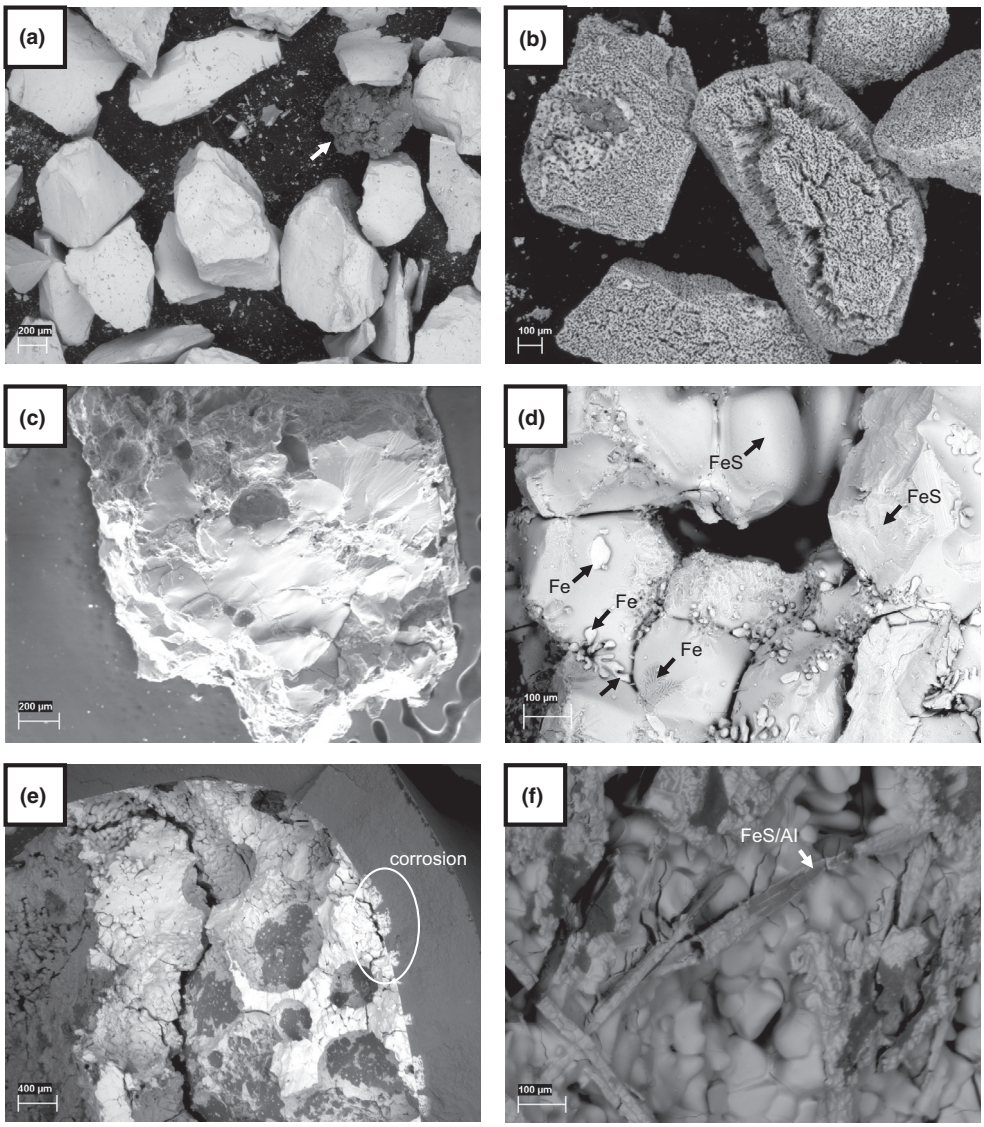

Fig. 5. Backscattered electron scanning electron microscope (SEM-BSE) images (density): (a) pyrite grains (TUG 1608- 6992-3) used for the decomposition to (b) pyrrhotite; (c, d) troilite grain (troilite1-2, troilite1-3), (e) troilite in its crucible (troilite2-2), and (f) troilite (troilite2-1). a) Among pyrite grains are found phyllosilicates (arrow) in very small amounts. b) Pyrrhotite grains are heavily decomposed, forming numerous cavities making the grains porous. c, d) Troilite crystal morphologies are various (angular or rounded surface) and sometimes show skeletal intergrowths and smaller inclusions of iron. Troilite is slightly reactive to the crucible and pitting occurs (circle in [e]), which can contaminate troilite with alumina particles such as seen in (f) where a crystal needle of troilite is contaminated by alumina (arrow). Such contamination in troilite only occurs close to contact with the crucible and is below detection level in X-ray diffraction analyses of retrieved troilite samples. Al = alumina-based minerals; FeS = iron sulfide-based minerals; Fe = iron-based minerals.

39.2 wt%), and troilite (troilite-2H) are confirmed with the XRD analyses. Only troilite spectra display a peak of iron contamination (~3%).

Compiled analyses of troilite (troilite3) from the troilite sample displayed in Fig. 4f are shown in Fig. 9. The crust layer was delicately handpicked in different places of the sample. Individual grains of troilite were selected and kept as obtained or hand-cleaned from the crust and possible alumina contamination. All analyses show iron contamination (~2–4%), and only in analyses of the uncleaned grains mullite contamination was detected, which is the ceramic material used for the crucible.

We detected slight quartz contamination (~3%) in the intermediate pyrrhotite of troilite4-1 and troilite5-1; we also detected iron silicon oxide contamination in pyrrhotite of troilite5-1 (<0.2%).

More thorough analyses of troilite4-1 melting yielded the following, with spectra compiled in Fig. 10

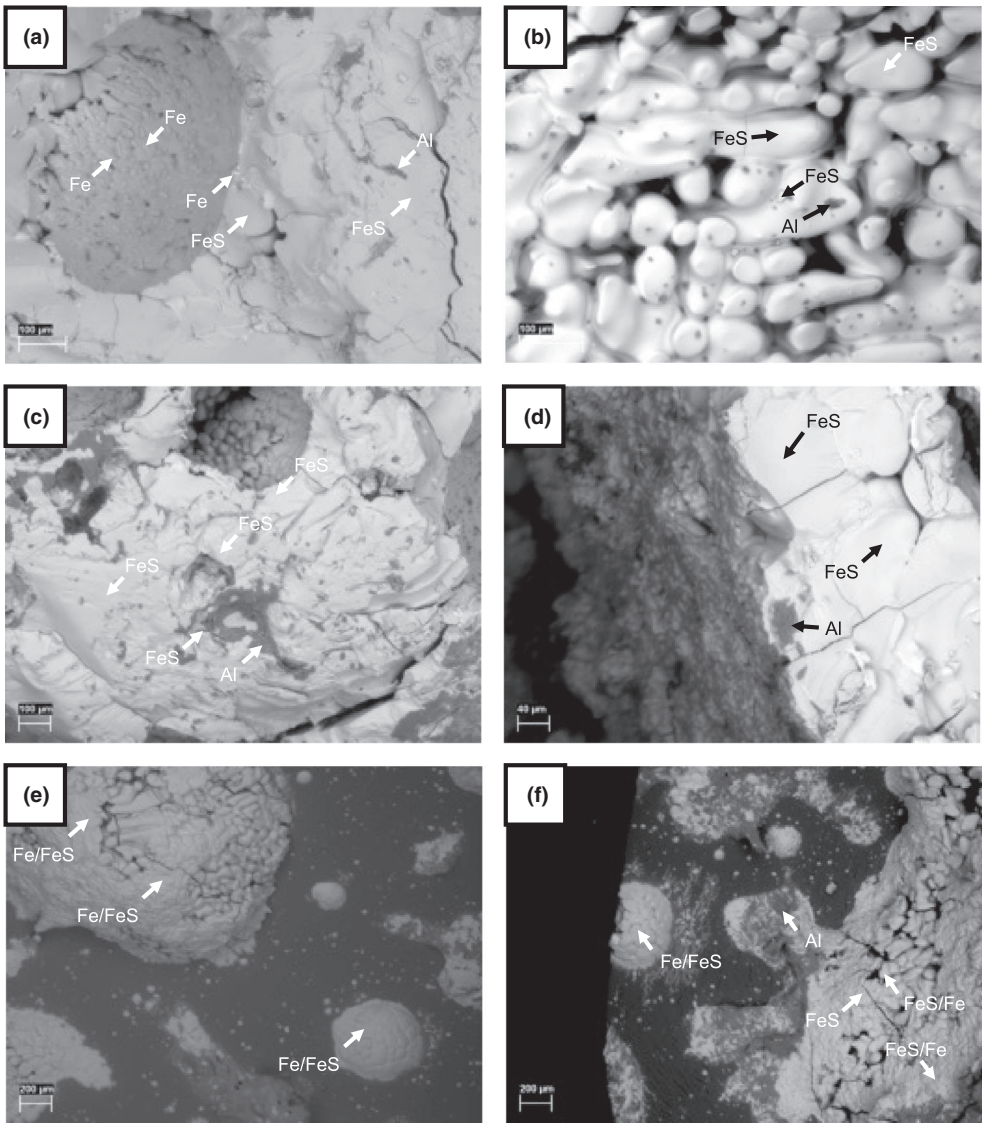

Fig. 6. Backscattered electron scanning electron microscope (SEM-BSE) images (density): (a) roughly angular troilite (troilite2-1), (b) rounded troilite (troilite2-3), (c) troilite with alumina contamination from contact to the crucible wall (troilite2-3), (d) formed crust of troilite (troilite2-2) from melting with slight alumina contamination, (e) crucible wall with iron contamination of troilite (troilite2-3), and (f) crucible wall with iron and alumina contamination of troilite (troilite2-2). Rounded, angular, or troilite from the crust often showed very little alumina contamination.

(see also Fig. 4 for given annotation and see the Decomposition and Melting section):

1. Troilite is confirmed for the material laying beneath the surface (Fig. 4f), away from the contamination of the needle-shaped minerals and other contamination mentioned earlier (see the SEM-BSE Observations section). For the picked grains, no iron or mullite was detected.
2. Surficial troilite is also confirmed for the material cleaned from major contamination; slight contamination of mullite and iron is detected in this case.
3. The cap element displayed in Fig. 4b.1 and Fig. 7a–c is composed in majority of mullite, and second, of rutile and troilite with slight iron contamination. Glass was also detected but was not analyzed for its composition.
4. The needles observed in Figs. 4b.2/3, 4d, 4e, 7d, and 7e are confirmed to be rutile crystals.
5. Other minerals that were analyzed from surface contamination in addition to the rutile minerals (Fig. 4b.2/3) are mullite, troilite, and, possibly, quartz.
6. The yellow material from the outlet of the oven is sulfur (Fig. 4c).

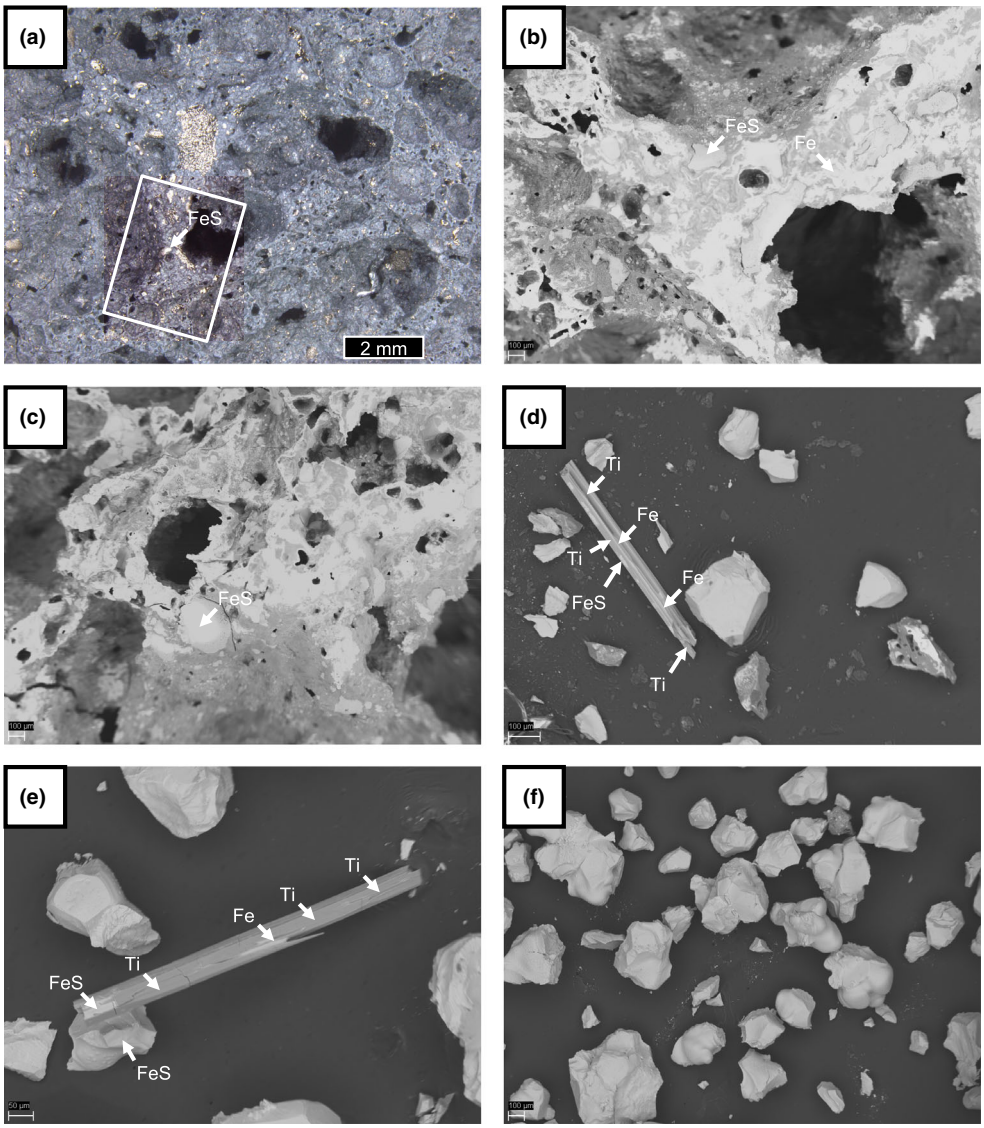

Fig. 7. Backscattered electron scanning electron microscope (SEM-BSE) images (density) of troilite4-1 test (Fig. 4): (a) microscope picture of a porous element, "cap" that sat atop the melt with troilite inclusions; (b, c) SEM picture of the porous element in (a) composed in majority of alumina minerals; (d, e) needle-shaped titanium oxide minerals that sat atop the melt; (f) troilite grains collected in the upper layer of the molten sample after cleaning of surface. The needle-shaped minerals also show inclusions/coating of iron and iron sulfide. Ti = titanium oxide-based minerals, FeS = iron sulfide-based minerals; Fe = iron-based minerals. The SEM image in (b) is highlighted in (a). (Color figure can be viewed at wileyonlinelibrary.com.)

In Situ High-Temperature X-Ray Diffraction (HTXRD)

HTXRD measurements were conducted on the pyrrhotite sample (troilite5-1) as described in the Analysis of Samples section. First, the major observation (Fig. 11) is the successful synthesis of troilite as previously seen in this work corroborated by diffractograms corresponding to pyrrhotite (PDF 29-726) before heating and troilite (PDF 37-477) after cooling. Second, peaks attributed to troilite appear when the mineral solidifies after being ~100 min in a liquid state from heating stage (~1373 K) to cooling stage (down to ~1223 K); several troilite peaks appear during the last steps of cooling, <423 K, consistent with the change from the MnP-type structure to the space group (P $\bar{6}$ 2c) (Oshtrakh et al., 2016). Finally, the troilite iron contamination observed earlier in this work is depicted by a peak appearing right at the crystallization of the troilite. Peaks appearing at the troilite liquid state are believed to be from the alumina crucible and from a hercynite phase $FeAl_2O_4$ possibly formed by reaction between the sample and the crucible. Any peak shifts

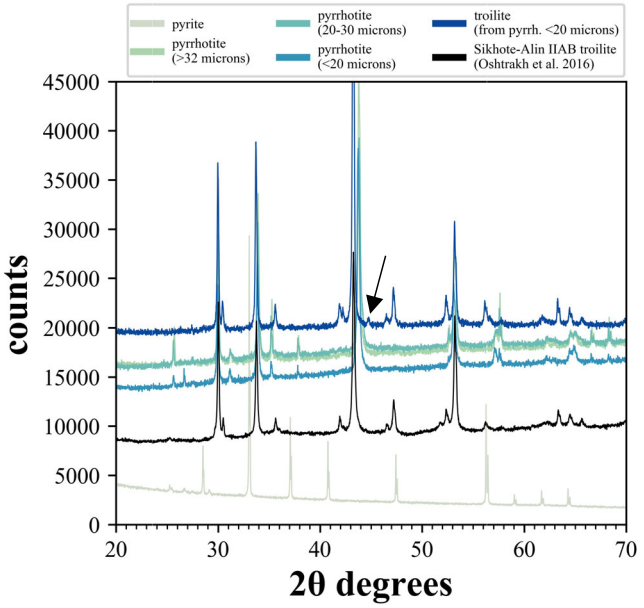

Fig. 8. X-ray diffraction analyses in 2-theta degrees showing the changes in composition of each product to form troilite (troilite1-1,2,3) with: spectrum for pyrite, spectra from the size-sorted pyrrhotite grains (matching PDF card 00-029-0726 for pyrrhotite-11T) after pyrite decomposition at 1023 K, and spectrum of troilite (matching PDF card 04-002-0919 for troilite-2H) after heat treatment and melting at 1498 K of the pyrrhotite grains. A comparative spectrum of Sikhote-Alin IIAB troilite (+ daubreelite contamination) from Oshtrakh et al. (2016) that fits the spectrum of synthesized troilite confirms the meteoritic-like composition of the latter. Weak iron contamination in troilite is detected in X-ray diffraction (3%, black arrow). The major difference between pyrrhotite and troilite X-ray diffraction spectra is the shift of the major peak from ~43.8°2θ to ~43.2°2θ. (Color figure can be viewed at wileyonlinelibrary.com.)

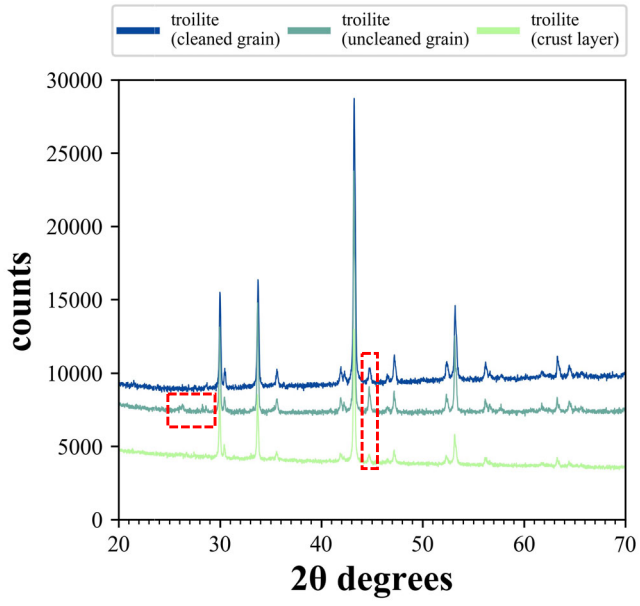

Fig. 9. X-ray diffraction analyses in 2-theta degrees of synthesized troilite (troilite3) matching PDF card 04-002-0919 for troilite-2H. Three samples are analyzed, after the sample shown in Fig. 3f: cleaned grain (crust layer and eventual crucible elements were removed by hand), uncleaned grain, and crust layer. Each sample has weak iron contamination (PDF card 04-016-6564), right-hand red box, which rules out external contamination in favor of iron exsolutions. Only the uncleaned sample is weakly contaminated by the alumina crucible with peaks matching the mullite mineral from PDF card 01-083-1881, left-hand red box. (Color figure can be viewed at wileyonlinelibrary.com.)

during heating or cooling are due to the combination of sample displacement and thermal extension in the oven. While the thermal expansion behavior is very interesting, it is beyond the scope of this paper and already partially explained, for example, in Selivanov et al. (2008), although using a narrower temperature range. A few peaks remain unidentified; they could either be oxidation from accidental exposure of the sample to air prior to measurements or the possible presence of greigite, a common mineral inclusion of pyrite (Akhtar et al., 2013).

DISCUSSION

Our results illustrate the successful synthesis of pyrite to troilite with a two-step thermal treatment where pyrrhotite is the intermediate product. Any test allowed us to synthesize troilite, in large quantities, as shown by XRD analyses and with only slight contaminations of iron and/or alumina. The alumina contamination is believed to come from sulfur corrosion of the crucible in which pyrrhotite is melted (sulfur escapes the system). The contamination remained mostly at the contact between the walls of the crucible and troilite or as a "floating cap," or slag on top of the melt, when large quantities of pyrrhotite were used for melting (troilite4-1). The slag possibly formed from a combination of degassing and corrosion (owing to the reducing environment) and floated on top of the melt. In contrast, there was no observation of denser elements at the bottom of the melt (e.g., chromium oxides). The appearance of needle-shaped crystals of alumina within troilite at crucible walls may be a result of such contamination via redox reaction as well. The contamination of iron exsolution is possible as iron and iron sulfide coexist as a solid solution. The degree of iron contamination is constant for most experiments within different troilite samples (except the sublayer troilite for troilite5-1 where iron was not detected), which is not systematic for alumina contamination. The observation of iron exsolution droplets is also observed in cavities within troilite, where N_2 was possibly trapped during melting of pyrrhotite to troilite. Iron is,

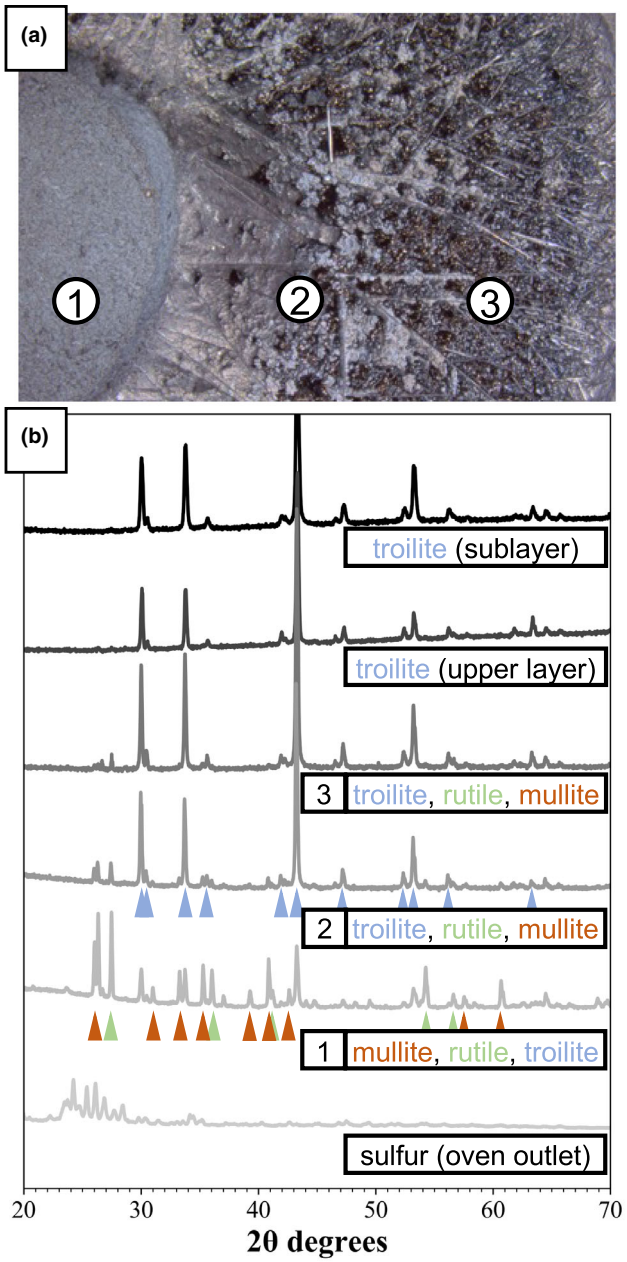

Fig. 10. X-ray diffraction analyses in 2-theta degrees of synthesized troilite (troilite4) and the surficial contaminants of the melt. Six samples are analyzed, after the sample shown in Figs. 4b–f, including three contamination zones depicted in (a). In order of appearance in (b): troilite grains that were cleanly retrieved from the crucible (Fig. 4f); troilite grains that were taken from the upper layer of crystallized melt; the outward upper layer of contaminations (3; Fig. 4e); the inward upper layer of contaminations (2; Fig. 4d); the gray cap atop the contaminated layer (1; Fig. 4b); and the sulfur deposit from the oven outlet (Fig. 4c). The major peaks for minerals and corresponding colored labels are shown as plain triangles in (b). Numerical annotations in (b) refer to those annotations in (a). Troilite has a sulfur content of 36–38 wt%. Relevant mineral labels are sorted by their percentage of detection when >1%. Quartz is detected in 1, 2, and 3; iron is detected in 1 and 2, and also in the upper layer troilite with a value of 1.34%. (Color figure can be viewed at wileyonlinelibrary.com.)

therefore, a by-product of troilite synthetization and should appear during the cooling of the troilite melt (Tomkins, 2009). The presence of iron in the final product will affect the eutectic properties of the troilite and iron mixture by lowering the melting point (Mare et al., 2014). Finally, the titanium oxide minerals (rutile) are only observed atop the melting crust of troilite4-1, indicating the pyrite minerals had a certain amount of titanium to start with. They also grew from and outward the crucible or alumina minerals, suggesting a dissolution–reprecipitation mechanism necessary for such needle-shaped minerals to form (Hwang et al., 2007). This contamination was not observed in the 17.34 g of recovered troilite from troilite4-1 test. Indeed, using large quantities of pyrrhotite for melting yields better qualitative results of troilite products. Using Ar or N_2 atmospheres in the highest temperature oven did not affect our results.

The XRD patterns of the experimental products match those of meteoritic troilite exactly (iron meteorite troilite inclusion; Oshtrakh et al., 2016). We observed a shift of the major peak between pyrrhotite and troilite, from ~43.2°2θ to ~43.8°2θ. Interestingly, within the troilite synthesis study of Onufrienok et al. (2020), we cannot safely state that the peak shift we observe in their XRD data for troilite after thermal treatment is comparable with the peak shift observed between pyrrhotite and troilite in our own XRD data (Fig. 8); as a note, the thermal treatment for troilite conversion was not complete in their case. Formation of troilite is also illustrated in our HTXRD analyses. Troilite is formed during cooling of the molten precursor solid phase with final peaks appearing <423 K, a change of crystal structure typical to genuine troilite. The mineral is not readily solidified from 1473 K but rather solidifies only at ~1223 K. As stated, the exsolution of iron appears to be an effect of cooling to troilite. Also, the synthesized troilite has a brownish-gold appearance, which is consistent with its appearance in unaltered meteorites (e.g., Oshtrakh et al., 2016; Ray et al., 2016), an important aspect for studying spectral properties of troilite powders (Dibb et al., 2021) if iron contamination is absent (e.g., troilite4-1 deep layer in our experiments, Fig. 4f). As for most recent studies, scientists either used troilite out from iron meteorites (Dibb et al., 2021) to have the most spectrally genuine elements or they purchased synthesized FeS powder (Prince et al., 2020). In the latter case, the FeS powder

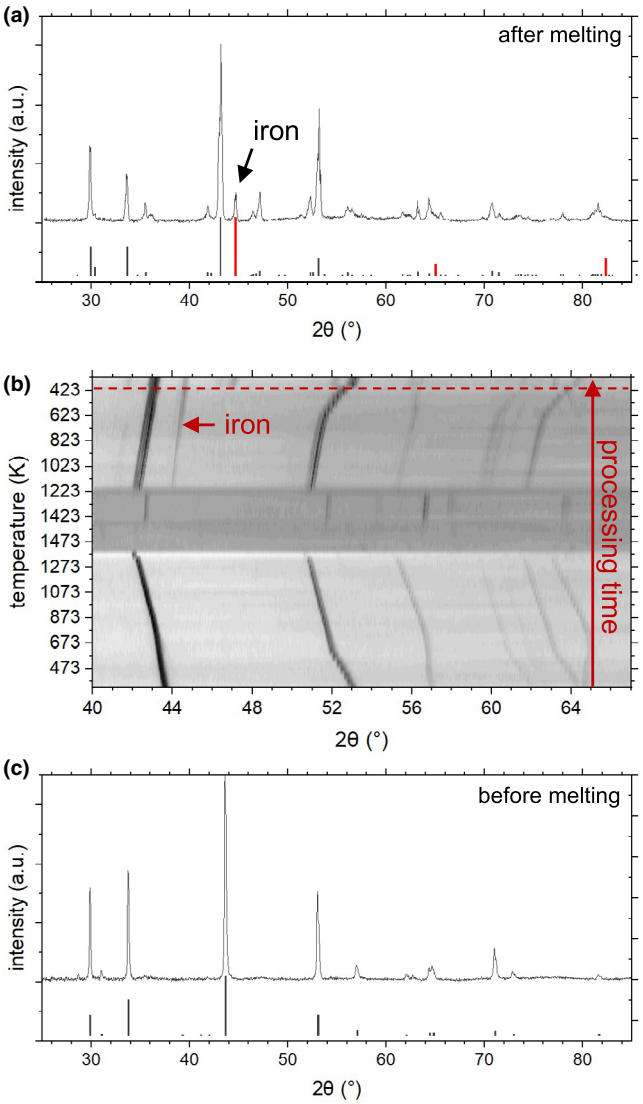

Fig. 11. In situ high-temperature X-ray diffraction analyses in 2-theta degrees of synthesized troilite (troilite5-1) in function of temperature (heating, melting, cooling) with (a) final X-ray diffraction spectra of synthesized troilite at room temperature, (b) 2-theta degrees in function of temperatures with peak intensities, and (c) the starting pyrrhotite material X-ray diffraction spectra at room temperature. Dashed red line in (b) highlights a change of troilite crystal structure. Arrows point at iron peaks. Processing time of the analysis starts from bottom of graphic (b). (Color figure can be viewed at wileyonlinelibrary.com.)

used in the study does not show the typical brownish-gold appearance that is usually observed in genuine troilites (see this work Figs. 3b,d and 4f). Therefore, commercial samples that are usually not provided with a structural analysis to identify the mineral phase unambiguously must be handled with care depending on the scientific question that is investigated.

Our synthesized troilite is easily reusable for dedicated experiments (e.g., reflectance spectra analyses and shock recovery experiments) if it is properly extracted from the crucible wall to avoid alumina contamination; this contamination can easily be avoided by producing larger quantities of troilite which, then, yield better purity levels. However, the iron contamination may impact properties of troilite such as a reduced Fe-FeS eutectic melting temperature (Mare et al., 2014) or changes in reflectance spectra properties (Dibb et al., 2021). Such contamination may possibly be prevented by assuring more control on the melting environment (gas flow, trapped gas, better preparation of pyrrhotite), on the contamination from corrosion by using crucibles with similar thermal resistance but better corrosion resistance (e.g., tungsten), and by retrieving troilite farther away from surface contamination and crucible walls.

CONCLUSION

We synthesized troilite in large quantities (e.g., 17 g from an initial weight of pyrite of 27 g). The troilite product matched with XRD analyses of meteoritic troilite. The production of meteoritic troilite is a major asset for planetary science research, especially for those interested in shock metamorphism of chondrites or metallic meteorites and spectral analyses of planetary surfaces and space weathering. Our synthesized troilite may present a slight contamination in iron, which will lower the troilite melting temperature; this is not a disadvantage as it may help establish shock recovery experiments to study melting of troilite by lowering its melting temperature. The procedure we propose is simple and only requires fresh pyrite. The two-step heating process allowed us to observe the transition between pyrrhotite product and troilite product, which is marked by the shift of the ~43.2°2θ to ~43.8°2θ peaks in XRD; we also offered direct observations of the mineral grains under electron microscope, depicting their morphology and the chemical reactions that may happen upon heating within the grains or the alumina crucible.

Acknowledgments—We gratefully thank the University of Tartu Natural History Museum for lending us the pyrite samples for troilite synthesis. We also thank Anu Adamson for helping to use the oven at the Institute of Chemistry, University of Tartu, and Marian Külaviir for assistance with the SEM-BSE analyses at the Department of Geology, University of Tartu. The HTXRD work was carried out using the ALD center Finland research infrastructure. We are also grateful for the precious comments provided by reviewer Prof. Lutz Hecht.

Funding—This work was supported by the European Regional Development Fund and Mobilitas Pluss programme (Grant No. MOBJD639).

Data Availability Statement—We provide XRD raw data and selected SEM-BSE images with qualitative spectral analyses as online Mendeley Data: https://doi.org/10.17632/6td5jtmwrn.1.

Editorial Handling—Dr. Natalia Artemieva

REFERENCES

Akhtar, M., Malik, M. A., Tuna, F., and O'Brien, P. 2013. The Synthesis of Iron Sulfide Nanocrystals from Tris(O-alkylxanthato)Iron(III) Complexes. *Journal of Materials Chemistry A* 1: 8766. https://doi.org/10.1039/c3ta12178j.

Boyabat, N., Õzer, A. K., Bayrakçeken, S., and Gülaboğlu, M. Ş. 2003. Thermal Decomposition of Pyrite in the Nitrogen Atmosphere. *Fuel Processing Technology* 85: 179–88. https://doi.org/10.1016/S0378-3820(03)00196-6.

Britt, D. T., and Pieters, C. M. 1989. Bidirectional Reflectance Characteristics of Black Chondrite Meteorites (Abstract). 20th Lunar and Planetary Science Conference. p. 109.

Britt, D. T., and Pieters, C. M. 1994. Darkening in Black and Gas-Rich Ordinary Chondrites: The Spectral Effects of Opaque Morphology and Distribution. *Geochimica et Cosmochimica Acta* 58: 3905–19. https://doi.org/10.1016/0016-7037(94)90370-0.

Britt, D. T., Pieters, C. M., Petaev, M. I., and Zaslavskaya, N. I. 1989. The Tsarev Meteorite—Petrology and Bidirectional Reflectance Spectra of a Shock-Blackened L Chondrite. Proceedings, 19th Lunar and Planetary Science Conference. pp. 537–45.

Brown, J. M., Ahrens, T. J., and Shampine, D. L. 1984. Hugoniot Data for Pyrrhotite and the Earth's Core. *Journal of Geophysical Research* 89: 6041–8.

Coats, A. W., and Bright, N. F. H. 1965. The Kinetics of the Thermal Decomposition of Pyrite. *Canadian Journal of Chemistry* 44: 1191–5.

de Oliveira, E. M., de Oliveira, C. M., Sala, M. V. B., Montedo, O. R. K., and Peterson, M. 2018. Thermal Behavior of Pyrite in the CO_2 and N_2 Atmosphere for Obtaining Pyrrhotite: A Magnetic Material. *Materials Research* 21: e20170244. https://doi.org/10.1590/1980-5373-MR-2017-0244.

DeMeo, F. E., Binzel, R. P., Slivan, S. M., and Bus, S. J. 2009. Extension of the Bus Asteroid Taxonomy into the Near-Infrared. *Icarus* 202: 160–80. https://doi.org/10.1016/j.icarus.2009.02.005.

DeMeo, F. E., and Carry, B. 2014. Solar System Evolution from Compositional Mapping of the Asteroid Belt. *Nature* 505: 629–34. https://doi.org/10.1038/nature12908.

Dibb, S. D., Bell, J. F. III, and Garvie, L. A. J. 2021. Reflectance Spectra of Metal-Troilite Mixtures: Implications for M-/X-Type Asteroid Exploration (Abstract #2548). 52nd Lunar and Planetary Science Conference. CD-ROM.

Fujita, T., Kojima, H., and Yanai, K. 1999. Origin of Metal-Troilite Aggregates in Six Ordinary Chondrites. *Antarctic Meteorite Research* 12: 19–35.

Güldemeister N., Moreau J., Kohout T., Wünnemann K., and Luther R. 2021. High Pressure Shock Metamorphism in Rubble-Pile Asteroids Using Numerical Simulations. European Planetary Science Congress 2021, 13–24 September. EPSC2021-468. https://doi.org/10.5194/epsc2021-468.

Heymann, D. 1967. On the Origin of Hypersthene Chondrites: Ages and Shock Effects of Black Chondrites. *Icarus* 6: 189–221. https://doi.org/10.1016/0019-1035(67)90017-6.

Hirata, N., Kurita, K., and Sekine, T. 1995. Shock Experiments on Silicate-Metal-Sulfide Powder Mixture: Effect of Low Eutectic Temperature of Sulfide-Metal System. Proceedings, 28th Lunar and Planetary Science Conference. pp. 44–7.

Hutchison, R. 2007. *Meteorites: A Petrologic, Chemical and Isotopic Synthesis*. Cambridge, UK: Cambridge University Press.

Hwang, S. L., Yui, T. F., Chu, H. T., Shen, P., Schertl, H. P., Zhang, R., and Liou, J. G. 2007. On the Origin of Oriented Rutile Needles in Garnet from UHP Eclogites. *Journal of Metamorphic Geology* 25: 349–62. https://doi.org/10.1111/j.1525-1314.2007.00699.x.

Keil, K., Bell, J. F., and Britt, D. T. 1992. Reflection Spectra of Shocked Ordinary Chondrites and Their Relationship to Asteroids. *Icarus* 98: 43–53. https://doi.org/10.1016/0019-1035(92)90205-L.

Kohout, T., Gritsevich, M., Grokhovsky, V. I., Yakovlev, G. A., Haloda, J., Halodova, P., Michallik, R. M., Penttilä, A., and Muinonen, K. 2014. Mineralogy, Reflectance Spectra, and Physical Properties of the Chelyabinsk LL5 Chondrite—Insight into Shock-Induced Changes in Asteroid Regoliths. *Icarus* 228: 78–85. https://doi.org/10.1016/j.icarus.2013.09.027.

Kohout, T., Petrova, E. V., Yakovlev, G. A., Grokhovsky, V. I., Penttilä, A., Maturilli, A., Moreau, J.-G. et al. 2020. Experimental Constraints on the Ordinary Chondrite Shock Darkening Caused by Asteroid Collisions. *Astronomy & Astrophysics* 639: A146. https://doi.org/10.1051/0004-6361/202037593.

Kracher, A., and Sears, D. W. 2005. Space Weathering and the Low Sulfur Abundance of Eros. *Icarus* 174: 36–45.

Langenhorst, F., and Deutsch, A. 1994. Shock Experiments on Pre-Heated Alpha-Quartz and Beta-Quartz: I. Optical and Density Data. *Earth and Planetary Science Letters* 125: 407–20. https://doi.org/10.1016/0012-821X(94)90229-1.

Langenhorst, F., and Hornemann, U. 2005. Shock Experiments on Minerals: Basic Physics and Techniques. *EMU Notes Mineralogy* 7: 357–87.

Lehner, S. W., Buseck, P. R., and McDonough, W. F. 2010. Origin of Kamacite, Schreibersite, and Perryite in Metal-Sulfide Nodules of the Enstatite Chondrite Sahara 97072 (EH3). *Meteoritics & Planetary Science* 45: 289–303.

Louzada, K. L., Stewart, S. T., Weiss, B. P., Gattacceca, J., and Bezaeva, N. S. 2010. Shock and Static Pressure Demagnetization of Pyrrhotite and Implications for the Martian Crust. *Earth and Planetary Science Letters* 290: 90–101.

Lunning, N. G., Mccoy, T. J., Schrader, D. L., Nagashima, K., Corrigan, C. M., Gross, J., and Kracher, A. 2019. Lewis Cliff 86211 and 86498: Metal-Sulfide Liquid Segregates from a Carbonaceous Chondrite Impact Melt. *Geochimica et Cosmochimica Acta* 259: 253–69.

Mare, E. R., Tomkins, A. G., and Godel, B. M. 2014. Restriction of Parent Body Heating by Metal-Troilite Melting: Thermal Models for the Ordinary Chondrites. *Meteoritics & Planetary Science* 49: 636–51. https://doi.org/10.1111/maps.12280.

Matsumoto, T., Harries, D., Langenhorst, F., Miyake, A., and Noguchi, T. 2020. Iron Whiskers on Asteroid Itokawa Indicate Sulfide Destruction by Space Weathering. *Nature Communications* 11: 1–8.

McSween, H. Y. Jr., Bennett, M. E. III, and Jarosewich, E. 1991. The Mineralogy of Ordinary Chondrites and Implications for Asteroid Spectrophotometry. *Icarus* 90: 107–16.

Morard, G., Andrault, D., Guignot, N., Siebert, J., Garbarino, G., and Antonangeli, D. 2011. Melting of Fe–Ni–Si and Fe–Ni–S Alloys at Megabar Pressures: Implications for the Core-Mantle Boundary Temperature. *Physics and Chemistry Minerals* 38: 767–776. https://doi.org/10.1007/s00269-011-0449-9.

Morard, G., Sanloup, C., Fiquet, G., Mezouar, M., Rey, N., Poloni, R., and Beck, P. 2007. Structure of Eutectic Fe–FeS Melts to Pressures up to 17 GPa: Implications for Planetary Cores. *Earth and Planetary Science Letters* 263: 128–39. https://doi.org/10.1016/j.epsl.2007.09.009.

Moreau, J., Jõeleht, A., Plado, J., Hietala, S., Sharp, T., Stojic, A. N., Schwinger, S. et al. 2021. Injection of Molten Iron Sulfides and Metals into Rocks: Developing a Technique to Study Shock Melt Veins in Ordinary Chondrites (Abstract #1044). 52nd Lunar and Planetary Science Conference. CD-ROM.

Moreau, J., Kohout, T., and Wünnemann, K. 2017. Shock-Darkening in Ordinary Chondrites: Determination of the Pressure-Temperature Conditions by Shock Physics Mesoscale Modeling. *Meteoritics & Planetary Science* 52: 2375–90. https://doi.org/10.1111/maps.12935.

Moreau, J., Kohout, T., and Wünnemann, K. 2018. Melting Efficiency of Troilite-Iron Assemblages in Shock-Darkening: Insight from Numerical Modeling. *Physics of the Earth and Planetary Interiors* 282: 25–38. https://doi.org/10.1016/j.pepi.2018.06.006.

Moreau, J., Kohout, T., Wünnemann, K., Halodova, P., and Haloda, J. 2019. Shock Physics Mesoscale Modeling of Shock Stage 5 and 6 in Ordinary and Enstatite Chondrites. *Icarus* 332: 50–65. https://doi.org/10.1016/j.icarus.2019.06.004.

Moreau, J., and Schwinger, S. 2021. Heat Diffusion in Numerically Shocked Ordinary Chondrites and Its Contribution to Shock Melting. *Physics of the Earth and Planetary Interiors* 310: 106630. https://doi.org/10.1016/j.pepi.2020.106630.

Morlok, A., Hamann, C., Martin, D., Weber, I., Joy, K. H., Hiesinger, H., Wogelius, R., Stojic, A. N., and Helbert, J. 2020. Mid-Infrared Spectroscopy of Laser-Produced Basalt Melts for Remote Sensing Application. *Icarus* 335: 113410.

Onufrienok, V. V., Chzhan, A. V., Bondarenko, G. V., and Yurkin, G. Y. 2020. Transition of Metastable Pyrrhotites to a Stable Phase State. *Inorganic Materials* 56: 898–902. https://doi.org/10.1134/S0020168520090137.

Oshtrakh, M. I., Klencsár, Z., Petrova, E. V., Grokhovsky, V. I., Chukin, A. V., Shtoltz, A. K., Maksimova, A. A. et al. 2016. Iron Sulfide (Troilite) Inclusion Extracted from Sikhote-Alin Iron Meteorite: Composition, Structure and Magnetic Properties. *Materials Chemistry and Physics* 174: 100–11. https://doi.org/10.1016/j.matchemphys.2016.02.056.

Pedoussaut, N. M., and Lind, C. 2008. Facile Synthesis of Troilite. *Inorganic Chemistry* 47: 392–4. https://doi.org/10.1021/ic701636h.

Prince, B. S., Magnuson, M. P., Chaves, L. C., Thompson, M. S., and Loeffler, M. J. 2020. Space Weathering of FeS Induced via Pulsed Laser Irradiation. *Journal of Geophysical Research—Planets* 125: e2019JE006242. https://doi.org/10.1029/2019JE006242.

Ray, D., Ghosh, S., and Murty, S. V. S. 2016. On the Possible Origin of Troilite-Metal Nodules in the Katol Chondrite (L6–7). *Meteoritics & Planetary Science* 52: 72–88. https://doi.org/10.1111/maps.12742.

Roberts, D. M., Landin, A. R., Ritter, T. G., Eaves, J. D., and Stoldt, C. R. 2018. Nanocrystalline Iron Monosulfides Near Stoichiometry. *Scientific Reports* 8: 6591. https://doi.org/10.1038/s41598-018-24739-8.

Rochette, P., Lorand, J.-P., Fillion, G., and Sautter, V. 2001. Pyrrhotite and the Remanent Magnetization of SNC Meteorites: A Changing Perspective on Martian Magnetism. *Earth and Planetary Science Letters* 190: 1–12. https://doi.org/10.1016/S0012-821X(01)00373-9.

Schrader, D. L., Davidson, J., McCoy, T. J., Zega, T. J., Russell, S. S., Domanik, K. J., and King, A. J. 2021. The Fe/S Ratio of Pyrrhotite Group Sulfides in Chondrites: An Indicator of Oxidation and Implications for Return Samples from Asteroids Ryugu and Bennu. *Geochimica et Cosmochimica Acta* 303: 66–91. https://doi.org/10.1016/j.gca.2021.03.019.

Selivanov, E. N., Gulyaeva, R. I., and Vershinin, A. D. 2008. Thermal Expansion and Phase Transformations of Natural Pyrrhotite. *Inorganic Materials* 44(4): 438–42.

Sharma, R., and Chang, Y. 1979. Thermodynamics and Phase Relationships of Transition Metal-Sulfur Systems: Part III. Thermodynamic Properties of the Fe-S Liquid Phase and the Calculation of the Fe-S Phase Diagram. *Metallurgical and Materials Transactions B* 10: 103–8.

Stöffler, D., Hamann, C., and Metzler, K. 2018. Shock Metamorphism of Planetary Silicate Rocks and Sediments: Proposal for an Updated Classification System. *Meteoritics & Planetary Science* 53: 5–49. https://doi.org/10.1111/maps.12912.

Stöffler, D., Keil, K., and Scott, E. R. D. 1991. Shock Metamorphism of Ordinary Chondrites. *Geochimica et Cosmochimica Acta* 55: 3845–67. https://doi.org/10.1016/0016-7037(91)90078-J.

Tomkins, A. G. 2009. What Metal-Troilite Textures Can Tell Us About Post-Impact Metamorphism in Chondrite Meteorites. *Meteoritics & Planetary Science* 44: 1133–49. https://doi.org/10.1111/j.1945-5100.2009.tb01213.x.

Waldner, P., and Pelton, A. D. 2005. Thermodynamic Modeling of the Fe-S System. *Journal of Phase Equilibria and Diffusion* 26: 23–38. https://doi.org/10.1361/1547703052245.

Xie, X., Chen, M., Zhai, S., and Wang, F. 2014. Eutectic Metal + Troilite + Fe-Mn-Na Phosphate + Al-Free Chromite Assemblage in Shock-Produced Chondritic Melt of the Yanzhuang Chondrite. *Meteoritics & Planetary Science* 49: 2290–304.

Xu, H., Guo, X., Seaman, L. A., Harrison, A. J., Obrey, S. J., and Page, K. 2019. Thermal Desulfurization of Pyrite: An In Situ High-T Neutron Diffraction and DTA-TGA Study. *Journal of Materials Research* 34: 3243–53. https://doi.org/10.1557/jmr.2019.185.